JACS
JOURNAL OF THE AMERICAN CHEMICAL SOCIETY
pubs.acs.org/JACS
Article

Development of Near-Infrared Nucleic Acid Mimics of Fluorescent Proteins for In Vivo Imaging of Viral RNA with Turn-On Fluorescence

Jiaheng Zhang,[⊥] Huiyi Li,[⊥] Bin Lin, Xingyu Luo, Peng Yin, Ting Yi, Binbin Xue, Xiao-Lian Zhang, Haizhen Zhu, and Zhou Nie*

Cite This: https://doi.org/10.1021/jacs.1c04577
Read Online

ABSTRACT: GFP-like fluorescent proteins and their molecular mimics have revolutionized bioimaging research, but their emissions are largely limited in the visible to far-red region, hampering the in vivo applications in intact animals. Herein, we structurally modulate GFP-like chromophores using a donor−acceptor−acceptor (D−A−A′) molecular configuration to discover a set of novel fluorogenic derivatives with infrared-shifted spectra. These chromophores can be fluorescently elicited by their specific interaction with G-quadruplex (G4), a unique noncanonical nucleic acid secondary structure, via inhibition of the chromophores' twisted-intramolecular charge transfer. This feature allows us to create, for the first time, FP mimics with tunable emission in the near-infrared (NIR) region (Em_{max} = 664−705 nm), namely, infrared G-quadruplex mimics of FPs (igMFP). Compared with their FP counterparts, igMFPs exhibit remarkably higher quantum yields, larger Stokes shift, and better photostability. In a proof-of-concept application using pathogen-related G4s as the target, we exploited igMFPs to directly visualize native hepatitis C virus (HCV) RNA genome in living cells via their in situ formation by the chromophore-bound viral G4 structure in the HCV core gene. Furthermore, igMFPs are capable of high contrast HCV RNA imaging in living mice bearing a HCV RNA-presenting mini-organ, providing the first application of FP mimics in whole-animal imaging.

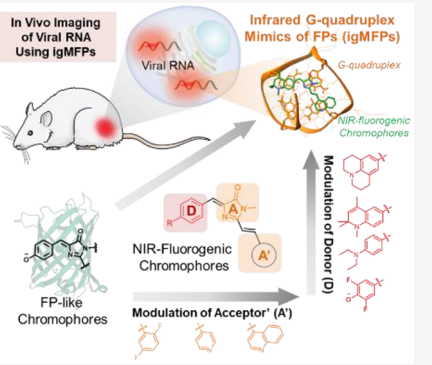

INTRODUCTION

Fluorescent proteins are revolutionary bioimaging tools that allow genetic tagging and dynamic monitoring of target proteins in living organisms.[1−3] Since the initial discovery of the green fluorescent protein (GFP), fluorescent proteins (FPs) have been constantly improved to meet the needs for advanced imaging applications.[4−6] An emerging demand is in vivo imaging in animals, which requires FPs to be emissive in the near-infrared (NIR) region to minimize endogenous autofluorescence, tissue absorbance and scattering, and phototoxicity.[6−8] Although genetic modifications of the GFP chromophore, 4-hydroxybenzylidene-imidazolinone (HBI), greatly expanded the color palette of FPs to the far-red, none of the GFP-derived FPs has exhibited emission maxima beyond 700 nm.[9−11] In 2009, the first example of NIR FP was developed based on the bacteriophytochromes binding with biliverdin, a chromophore completely independent of GFP-like ones.[12] However, how to implement emissive GFP-like chromophores in the NIR window is still an unsolved challenge to date.

Synthetic FP chromophores and their derivatives provide not only ideal models for exploring spectral behaviors of engineered FPs but unprecedented functional mimics of FPs to develop innovative imaging applications.[13−15] These chromophores are mostly nonfluorescent due to the rapid nonradiative decay arising from intramolecular rotations.[16,17] Inspired by the natural confined effect of FPs, several artificial FP mimics have been developed to elicit fluorescence of FP chromophores via restricting their rotation by intramolecular locking[18] or confinement in supramolecular cavities,[19] metal−organic frameworks,[20] and host proteins[21,22] or nucleic acids.[23] Given their precisely tunable photophysical properties and dual engineering of chromophores and hosts, these synthetic FP mimics provide promising toolkits for developing novel imaging methods.[24] Among them, nucleic-acids-based FP mimics are highly promising for bioimaging applications due to their biocompatibility, genetic-encoding feature, and highly specific structure adaptability.[25,26] In this regard, Jaffrey et al. developed a series of FP chromophores-activating aptamers to form RNA mimics of FPs and further exploited them as genetic tags for RNA imaging in living cells.[27,28] These pioneer works opened a door to the field of "fluorogenic RNA", which endows RNA a genetic-encoding fluorescent labeling system

Received: May 3, 2021

Scheme 1. Rational Design of the Infrared G-Quadruplex Mimics of FPs (igMFPs) for In Vivo Imaging of Viral RNA

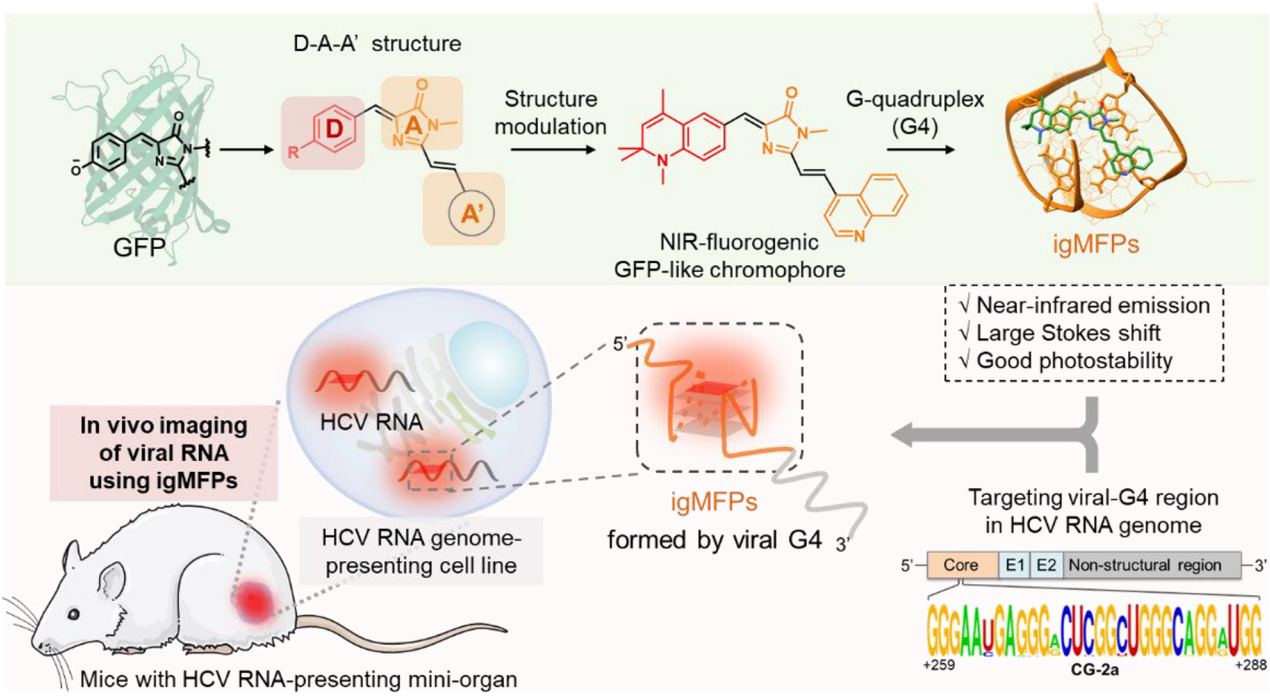

comparable to FPs as proteins.[29−32] Our group have previously demonstrated that encapsulating red fluorescent protein (RFP) chromophore analogues in canonical G-quadruplex (G4) structures can elicit bright fluorescence spanning the whole spectral range overlapping with natural RFPs.[33] However, analogous to GFP-like FPs, FP mimics' emission is still largely limited in the visible to far-red region, hampering the in vivo imaging application of FP mimics in whole animals. Therefore, it is highly desirable to overcome the intrinsic limitations of GFP-like FPs and their mimics to achieve highly efficient NIR emission for in vivo biomolecular imaging.

Herein, we describe a rational design strategy to create near-infrared mimics of FPs based on HBI-like chromophores with a donor−acceptor−acceptor (D−A−A′) molecular configuration (Scheme 1). By fine-tuning the electronic characters of donor and acceptor moieties, we structurally tailored the natural chromophore of a red-emissive FP, Kaede, and synthesized a set of D−A−A′ type analogues with infrared-shifted spectra, which are highly advantageous for in vivo biomolecular imaging.[34] Due to their conjugated π-ring system, these chromophores can be fluorescently elicited by their specific interaction with G-quadruplex, a unique noncanonical nucleic acid secondary structure with stacked multilayer G-quartets formed by G-rich sequences via Hoogsteen hydrogen bonding.[46] The G-quartet of G4 provides an ideal binding site for the chromophores to stack upon, therefore restricting them to a planar conformation for efficient emission. Compared with their parental FP Kaede (Em_{max} = 580 nm), these G4-chromophore complexes, termed infrared G-quadruplex mimics of FPs (igMFP), greatly expand the spectral palette to the near-infrared region with tunable emission maxima (664−705 nm), successfully surpassing the intrinsic limitations of existing GFP-like FPs and their mimics. Furthermore, these new igMFPs exhibit unexpected high quantum yields that are superior to all known FPs emissive at NIR region as well as several other extraordinary features, such as large Stokes shifts, excellent photostability, and efficient live-cell permeability. Moreover, the igMFP system is applicable for deep-tissue visualization and whole-body imaging in a live animal to monitor the innate noncanonical G-quadruplex (G4) structure embedded in the pathogenic RNA genome, i.e., the viral gene of hepatitis C virus (HCV). To the best of our knowledge, this is the first report of the molecular tailoring of the highly emissive NIR-emissive FP mimics capable of in vivo fluorescent imaging in living animals.

RESULTS AND DISCUSSION

D−A−A′ Type GFP-Like Chromophores with NIR-Emissive Fluorogenic Properties. The core chromophore of GFP, HBI, is a conjugated system composed of a phenol group (electron-donor, D) and an imidazolinone ring (electron-acceptor, A).[35] Inspired by the chromophore structure of Kaede, we previously developed a series of RFP chromophore derivatives via extending the π-system of HBI with styryl substitutes at the C2-position of the imidazolinone ring, e.g., DFHBFSI with maximum emission at 610 nm in its G4-bound state (shown in Figure 1A).[33] We also found that further extension of the π-rich bridge (from a vinyl group to an olefinic group) between the aromatic substitutes and imidazolinone ring leads to a significant bathochromic effect. However, it also dramatically diminishes the binding affinity and quantum yield of the HBI derivative when bound to G4, probably due to its oversized structure compared with a G-quartet. Therefore, we herein focus on fine-tuning the electronic structure of HBI derivatives without extending the π-rich linkage remarkably to achieve further expansion of emission maximum to the NIR region. Following this principle, we propose a unique asymmetric donor−acceptor−acceptor (D−A−A′) framework of HBI-based chromophores with rationally designed electron-donating D moieties and additional electron-withdrawing A′ moieties (Figure 1A). The D−A−A′-configured design rationale enables synergistic tuning of

https://doi.org/10.1021/jacs.1c04577
J. Am. Chem. Soc. XXXX, XXX, XXX−XXX

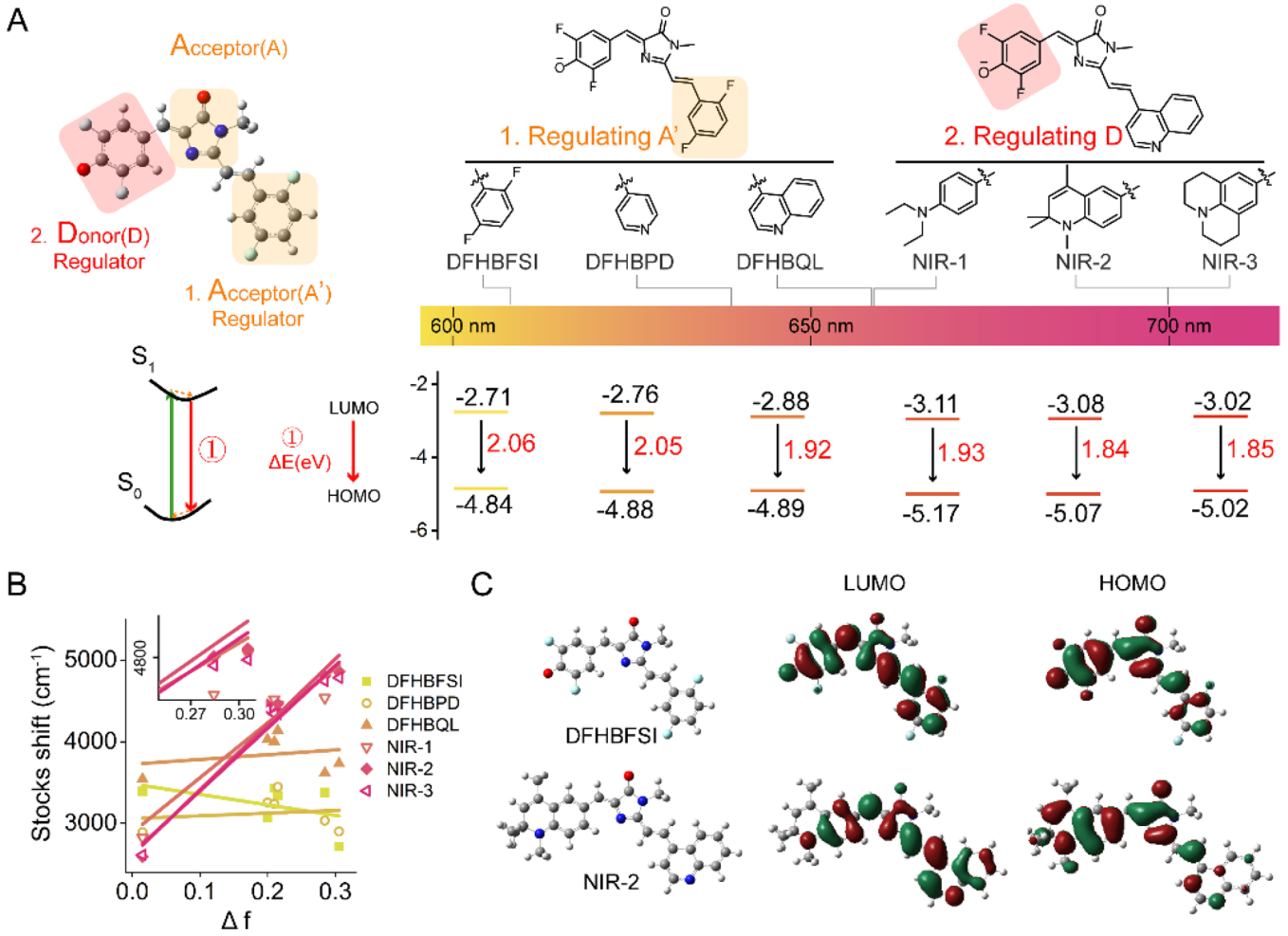

Figure 1. (A) Upper: Schematic illustration of the general strategies for tuning emission wavelength of FP-like chromophores and the maximum emission wavelength of them in ethanol. Lower: Calculated HOMO−LUMO energy levels and de-excitation energies (① ΔE) of DFHBFSI, DFHBPD, DFHBQL, NIR-1, NIR-2, and NIR-3, respectively, at the excited state. (B) Lippert−Mataga plots versus the solvent orientation polarizability (Δf) for FP-like chromophores. (C) The HOMO and LUMO orbitals of DFHBQL and NIR-2 at excited state and optimized excited state (S1).

the optical energy gap and enhances the photoinduced intramolecular charge transfer (ICT), leading to infrared-shifted spectra.

Guided by the D−A−A′ rationale, we synthesized a set of RFP chromophore analogues via an Erlenmeyer azlactone reaction or 2,3-cycloaddition followed by condensation with corresponding arylaldehydes. Detailed synthetic processes and characterization, including NMR and HRMS data, are shown in Schemes S1−S3 and Figures S1−S13. At first, the spectral effects of the electronic character of A′ moieties were investigated. As shown in Figure 1A, the substitutions of nitrogen-containing aromatic heterocycles (DFHBPD with pyridine and DFHBQL with quinoline) for 1,4-difluorobenzene of DFHBFSI cause a significant emission bathochromic shift (30 and 56 nm, respectively) in ethanol (Figure S14) due to their enhanced electron-withdrawing properties. The time-dependent density functional theory (TDDFT) calculations (at the B3LYP/6-31+G(d) level) indicated that these substitutions of A′ groups had a stronger stabilizing effect on LUMO than that on HOMO (Figure 1A and Figure S15), thus reducing the de-excitation energy gap (e.g., 1.92 eV for DFHBQL vs 2.06 eV for DFHBFSI) during the emission processes to achieve a spectral redshift. By comparison, we also replaced the A′ moiety of DFHBFSI with the electron-donating group (dialkylaminobenzene, DFHBASI) or a π excessive heterocycle (indole, DFHBID). We observed a remarkable emission hypsochromic shift (20 and 25 nm, respectively) in ethanol (Figure S14), corresponding to the increased de-excitation energy gap (e.g., 2.14 eV for DFHBASI vs 2.06 eV for DFHBFSI, Figure S16). This result further supports the significance of the electron-withdrawing properties of A′ moieties for emission redshift.

Subsequently, the electron-donating D group was optimized using DFHBQL as the starting compound. We replaced the difluorophenolic moiety of DFHBQL by various dialkylaminobenzyl groups (NIR-1/2/3 in Figure 1A) for two considerations: (1) the spectral redshift and quantum yields of HBI analogues are susceptible to protonation of their phenolic groups, and (2) dialkylamino groups para-substituted on aromatic rings are stronger and more tunable donating groups for spectral redshift.[36,37] As expected, all the chromophores display emission peaks in the NIR region in ethanol, especially NIR-2 and NIR-3 reaching 700 nm. The notable emission redshift of NIR-2/3 compared with NIR-1 is attributed to the $\pi-\pi$ conjugation of extra double bonds or the $p-\sigma$ hyperconjugation of the julolidine ring, consistent with

https://doi.org/10.1021/jacs.1c04577
J. Am. Chem. Soc. XXXX, XXX, XXX−XXX

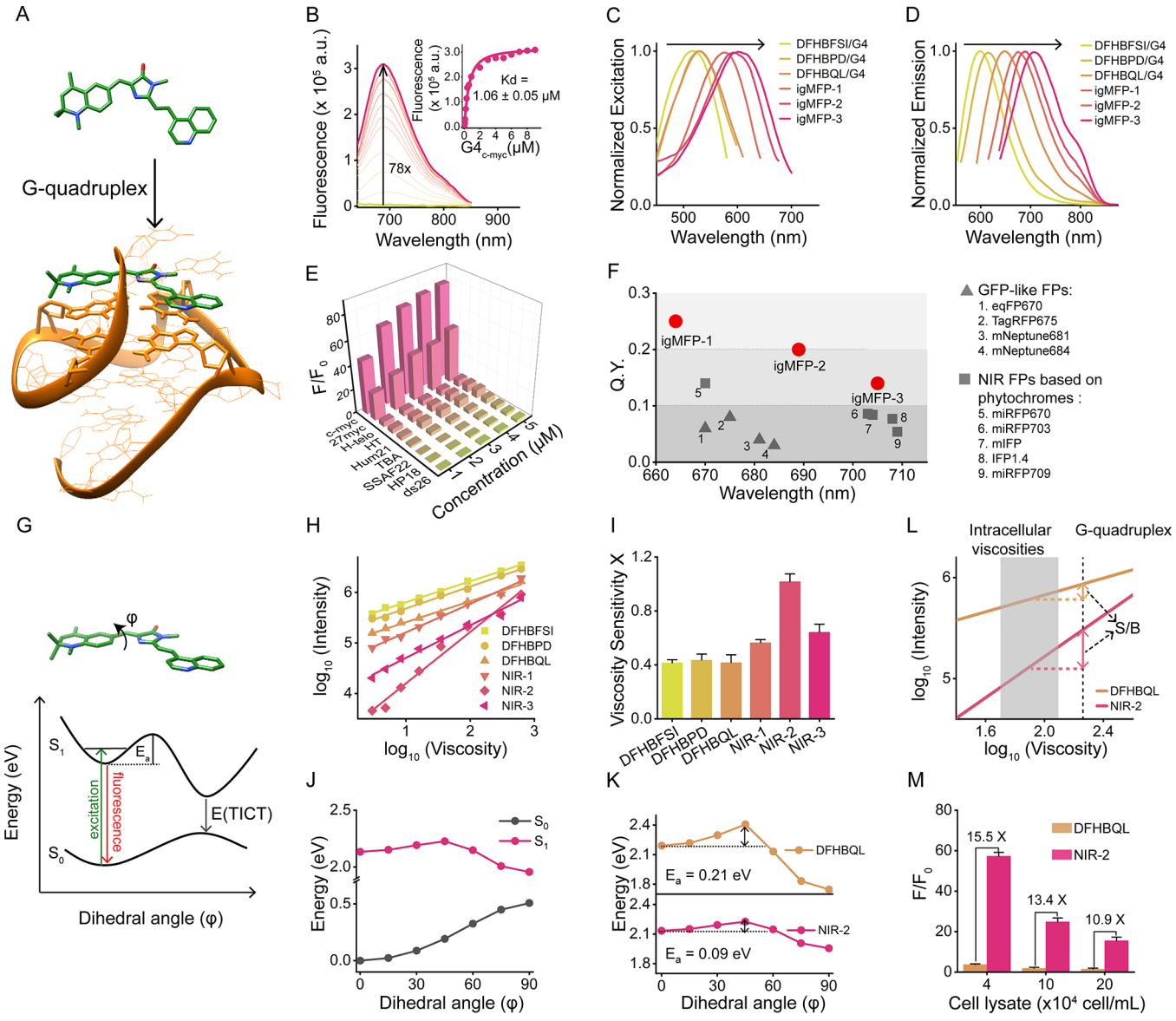

Figure 2. (A) Molecular docking of the NIR-2/G4 complex. (B) Emission spectra and fluorescence intensity change (insert) at 689 nm of NIR-2 (1 μM) upon stepwise addition of G4 $_{c\text{-}myc}$. (C) Excitation and (D) emission spectra of the FP-like chromophore-G4 $_{c\text{-}myc}$ complexes. (E) Changes in the fluorescence of NIR-2 (1 μM) in response to different nucleic acid structure, including parallel G4 (c-myc and 27myc), mix-type G4 (H-telo, HT, and Hum21), antiparallel (TBA), single-stranded (SSAF22), double-stranded (ds26), and hairpin (HP18). (F) Fluorescence quantum yields (Q.Y.) of igMFP-1, igMFP-2, igMFP-3, selected GFP-like FP and NIR FPs based on phytochromes. (G) Schematic illustration of TICT mechanisms. The Jablonski diagram shows that a NIR-2 molecule harbors a rotational barrier between the fluorescence state and the TICT state. (H) Linear fitting of double logarithmic plots of intensity versus viscosity of the indicated FP chromophores. (I) Viscosity sensitivity of different FP chromophores. (J) Potential energy surfaces of NIR-2 at the S1 and S0 states. (K) Potential energy surfaces of NIR-2 and DFHBQL at excited state. The excited state rotational barriers are calculated to be Ea = 0.09 eV (NIR-2) and Ea = 0.21 eV (DFHBQL), respectively. (L) Comparison of the differences in fluorescence signals of DFHBQL and NIR-2 between binding G4 and in the viscosity range of major intracellular organelles. (M) Changes in the fluorescence of DFHBQL (1 μM) and NIR-2 (1 μM) in response to G4$_{c\text{-}myc}$ (10 μM) in cell lysate.

their difference in de-excitation energy gaps (e.g., 1.84 eV for NIR-2 vs 1.93 eV for NIR-1) calculated by TDDFT (Figure 1A and Figure S17). Moreover, the detailed investigation on the solvatochromic effects indicates that NIR-1/2/3 exhibited increasing Stokes' shifts and decreasing fluorescence intensities with increasing solvent polarity (Figure S18). As depicted in the resulting Lippert−Mataga plots (Figure 1B), the higher slopes of NIR-2/3 than other HBI-derived chromophores suggest these optimized D−A−A′ type chromophores exhibit a higher polarized excited state and experience a stronger intramolecular charge transfer (ICT) process. The electron density analysis of NIR-2 showed a significant electron redistribution from the HBI-like core in the HOMO to the imidazolinone ring and its conjugated diarylethene group in the LUMO (Figure 1C), confirming the strong ICT process in their locally excited (LE) states involved in the rationale of the observed large Stokes shift (up to 157 nm measured in ethanol).[38] Further comparison with DFHBFSI revealed that NIR-2 experiences stronger electron delocalization than DFHBFSI in the LE state, supporting the chromophore tailoring by the D−A−A′ rationale enhancing the ICT process.

https://doi.org/10.1021/jacs.1c04577
J. Am. Chem. Soc. XXXX, XXX, XXX−XXX

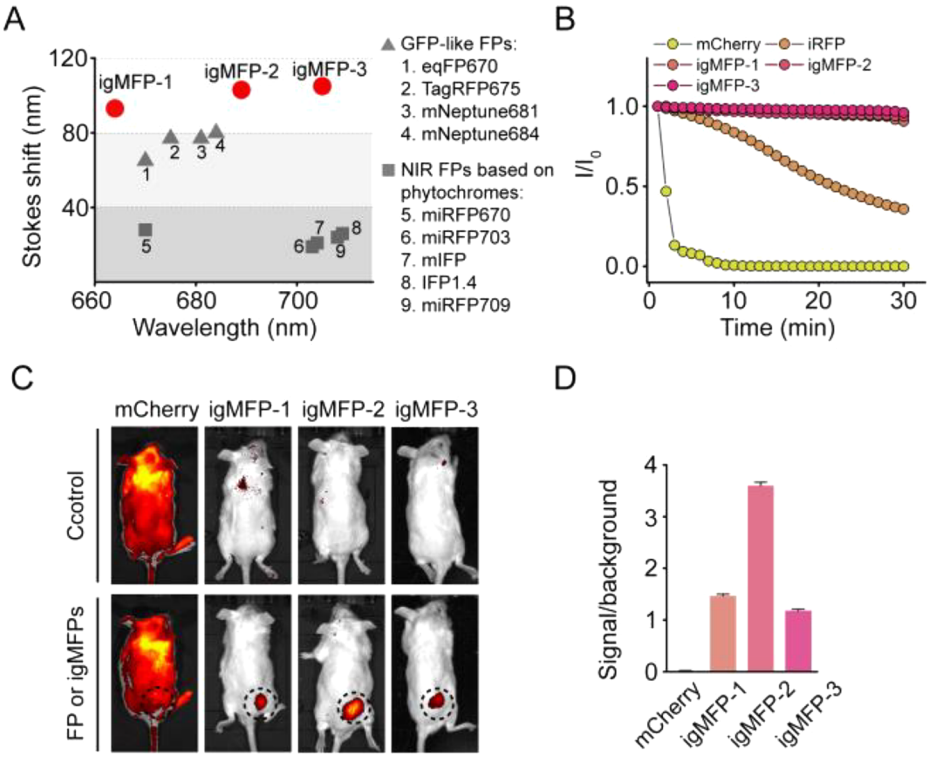

Figure 3. (A) Stokes shifts of igMFP-1, igMFP-2, igMFP-3, selected GFP-like FP, and NIR FPs based on phytochromes. (B) Photobleaching curves of 1 μM igMFP-1, igMFP-2, igMFP-3, mCherry, and iRFP, respectively. In vivo fluorescence images (C) and signal-to-background ratios (D) of 5 μM mCherry, igMFP-1, igMFP-2, and igMFP-3 with the same volumes (100 μL), respectively, injected into the mouse subcutaneous tissue. Values represent means ± SD (n = 3).

Spectrally Tunable igMFPs Formed by G4-Bound NIR-Emissive FP-Like Chromophores. Next, we investigate whether these NIR-emissive FP chromophore analogues were fluorescently activatable by interaction with G-quadruplex. Taking a G4-forming DNA sequence from c-myc gene promotor[39] (c-myc) as the model (Figure 2A), we found that although the NIR-1/2/3 alone are nonfluorescent in aqueous buffer solutions, the G-quadruplex structure can efficiently activate the fluorescence of NIR-1/2/3 to form the infrared G-quadruplex mimics of FPs. For instance, the binding with $G4_{c\text{-}myc}$ induced a 78-fold fluorescence enhancement of NIR-2, and the detailed fluorescence titration analysis indicated a 1:1 binding model for the NIR-2/$G4_{c\text{-}myc}$ complex (namely, igMFP-2) with a good affinity (K_d = 1.06 ± 0.05 μM) (Figure 2B and Figures S19 and S20). This fluorescence-activating effect is highly structure-specific to parallel G4 structures (c-myc and 27myc) and was negligibly observed in mix-type (H-telo, HT, and Hum21) or antiparallel G4s (TBA), single-stranded (SSAF22), double-stranded (ds26), and hairpin (HP18) nucleic acid structures (Figure 2E and Figures S21 and S22). The igMFPs can be spectrally tuned with emissive peaks ranging from 664 to 705 nm by simply changing NIR-emissive FP chromophore derivatives (Figure 2C,D and Figure S23). It is interesting to note that in igMFPs, NIR-2 shows a moderate hypsochromic shift of emission maxima (689 nm), but NIR-3 further redshifts to 705 nm in comparison with their identical emission (Em_{max} = 700 nm) in ethanol. Moreover, upon binding with G4, the emission maxima of their difluorophenol-bearing counterparts (DFHBFSI, DFHBPD, and DFHBQL) exhibited obvious blueshifts relative to those in ethanol, all located in the far-red region (600−648 nm). Unexpectedly, the complexes of G4 and NIR-1/2/3, namely, igMFP-1/2/3, were highly emissive with quantum yields of 0.25 (Em_{max} = 664 nm), 0.20 (Em_{max} = 689 nm), and 0.14 (Em_{max} = 705 nm), respectively, which is much higher than those of all existing FPs with emission maxima above 660 nm, such as GFP-derived TagRFP675 (0.08) and bacteriophytochromes-derived miRFP709 (0.05) (Figure 2F and Tables S2 and S3).

Because synthetic FP chromophore derivatives are typical molecular rotors, their fluorescence enhancement requires the restriction of their intramolecular movement[40,41] (Figure 2G). Given that molecular rotors are viscosity-sensitive in general[42] and the proposed D−A−A′ type chromophores with strong ICT character are also polarity-sensitive, the subtle spectral features of igMFPs will provide more detailed information about the G4−chromophore interaction microenvironment. To investigate the molecular rotor property of NIR-1/2/3, we measured their viscosity response in different glycerol−water mixtures (Figure 2H). The remarkable fluorescence enhancement with increasing viscosity was observed in all chromophores, in which NIR-2 shows the highest viscosity sensitivity (x = 1.02), much higher than other chromophores (x = 0.41−0.64, Figure 2I). The DFT calculations (at the B3LYP/6-31+G(d) level) of NIR-2 and DFHBQL were carried out to elucidate this distinction in viscosity sensitivity. DFHBQL was chosen for comparison because of its structural similarity to NIR-2 except for the variant D moiety and the representative viscosity sensitivity comparable to other chromophores. The calculation results indicated that both NIR-2 and DFHBQL exhibit similar profiles of potential energy surface scans (Figure 2J and Figure S24), in which the relaxation of the excited chromophores (S1) starts with internal rotation and then approach the point of the minimum energy conical intersection

https://doi.org/10.1021/jacs.1c04577
J. Am. Chem. Soc. XXXX, XXX, XXX−XXX

between S1 and S0 when the twist angle (φ angle in Figure 2G,J and Figure S24) about the phenyl (P) single bond reaches 45°, causing the twisted intramolecular charge transfer (TICT)-induced nonradiative decay.[43,44] However, in term of the excited state rotational energy barrier, a key factor determining the viscosity sensitivity of molecular rotors, NIR-2 possesses a lower barrier (Ea is 0.09 eV for NIR-2 and 0.21 eV for DFHBQL, Figure 2K), implying that compared with DFHBQL, NIR-2 can transform more readily into TICT state and require higher viscosity to restrict its rotation, thus being more sensitive to viscosity change. Accordingly, we propose two inferences: (1) the intramolecular motions of NIR-1/2/3 chromophores could be largely inhibited by their binding with G-quadruplex, inducing a significant fluorescence enhancement (e.g., 78-fold for NIR-2) comparable to that caused by a high-viscosity environment (~178 cP for NIR-2); (2) given that the viscosities of major intracellular organelles range from 50 to 130 cP,[45] the chromophores possessing higher viscosity sensitivity would recognize G4 with higher sensitivity and selectivity and induce less background caused by intracellular constituents (Figure 2L). To corroborate this hypothesis, we prepared a mimicking system with $G4_{c\text{-}myc}$ supplemented in cell lysate (2×10^5 cell/mL, eliciting a background fluorescence comparable to the intracellular viscosity of ~74−80 cP) and found that the signal to background ratio (S/B) of NIR-2 is about 11-fold higher than that of DFHBQL (Figure 2M), suggesting that the NIR chromophore with high viscosity sensitivity is promising for high-contrast live-cell imaging.

Notably, these igMFPs possess pronouncedly large Stokes shifts of 94, 98, and 105 nm for NIR-1/2/3, respectively, significantly larger than all NIR-emissive FPs (normally 10−20 nm, Figure 3A and Tables S2 and S3), including the Stokes-shift-extended variant TagRFP675 (77 nm), implying that igMFPs are advantageous for high-contrast imaging with less self-quenching and excitation backscattering interference. Interestingly, the Stokes shifts of G4-bound NIR-1/2/3 were considerably smaller than those in ethanol, resulting from their G4 binding-induced bathochromic shift of the excitation maxima (Table S4), which is likely due to the increasing coplanarity of the S_0 geometries by G4 confinement (detailed illustration was shown in Figure S25). Next, we examined the photostability of the proposed NIR FP mimics. The fluorescence of igMFPs shows a negligible decrease upon continuous irradiation over 30 min. However, the fluorescence intensity dropped by 40% for iRFP, a bacteriophytochromes-derived NIR FP, and 80% for mCherry, a representative RFP, suggesting that igMFPs have a better photostability against photobleaching (Figure 3B). The superior photostability of igMFPs was probably due to its noncovalent interaction diminishing the accumulation of photobleached complexes via the partial exchange of bound chromophore with a free one in solution (Figure S20). Furthermore, the advantage of NIR imaging with intrinsically deeper penetration was also examined in a simulated deep-tissue setting. We imaged igMFP-1/2/3 and mCherry in mouse subcutaneous tissue, and the signal-to-background (S/B) ratio for them was calculated for each channel. As shown in Figures 3C,D, compared with mCherry with significant intrinsic background interference from tissue, all igMFPs have remarkably larger S/B values, and igMFP-2 shows the highest ratio. Taken together, NIR-2 was chosen as the model chromophore for further biological applications because of its highest brightness, even ~2.8-fold brighter than NIR-3 when emission at 705 nm in igMFPs (Figure S26), much less intracellular background interference due to its highest viscosity sensitivity, as well as the highest contrast in deep-tissue imaging.

Lighting Up Viral G4s with NIR-Emissive FP-Like Chromophores to Form igMFPs. Inspired by the important role of FPs as bioimaging tags in living systems, we further explored whether our NIR mimics of FPs could be employed as fluorescent probes to track biomacromolecules in cells and even in vivo. G4 structures have a wide range of biological significance and are thought to be involved in regulating diverse biological and pathological processes.[46−51] For instance, recent studies have proved that the putative G4 sequence was present in the genomes of various RNA viruses, and the formation of G4 motif plausibly participates in viral infectivity and transcription.[52−55] Currently, we proposed the potential role of the innate virus genomic G4 structure as a specific target for viral RNA imaging and demonstrated its feasibility via the visualization of the hepatitis C virus (HCV) RNA genome in live host cells by the G4-specific probes targeting to its viral G4 sequence.[56] In light of their prominent NIR-spectral merits, G4 structure-specific fluorogenic property and high G4-binding affinity, we sought to exploit our FP-derived chromophores with NIR emission to light up innate viral G-quadruplex structure via forming igMFPs, thus allowing imaging of native HCV RNA genome not only in living cells but also further expandable to the whole-body level.

Accordingly, we chose HCV subtype 2a, the predominant HCV genotype in China, as a model and selected its highly conserved putative G4 sequence (5′-GGGAAUGAGGGACU-CGGCUGGGCAGGAUGG-3′), namely, CG2a, located at the position between +259 and +288 of the HCV core gene as the target. The HCV core gene encodes the Core protein, a highly conserved structural protein essential for the virus nucleocapsid formation. The 30 nt CG2a RNA sequence was synthesized for evaluating the formation of igMFPs based on the NIR-2/CG2a complex in vitro (Figure 4A). As indicated by the circular dichroism (CD) spectrum, CG2a can form a parallel G4 topological structure (Figure S27). Upon binding to CG2a, NIR-2 has a significant fluorescence enhancement but shows negligible fluorescence upon the addition of mutated CG2a sequences (CG2a-Mut and CG2a-Mut2) owing to partial G-A mutations of the CG2a sequence hindering the formation of G4 (Figure S28). NIR-2 also exhibits little fluorescent response to other RNA conformations, including single-stranded, double-stranded, hairpin, tRNA fragment, and extracted total cellular RNA (Figure S29), and other predominant cell constituents involving duplex DNA, amino acids, and proteins (Figure S30). Further quantitative analysis by fluorescence titration experiments indicated NIR-2 binds with CG2a to form igMFPs in a 1:1 mode (Figure S31) with a good affinity (K_d = 1.58 ± 0.18 μM) (Figure S32), thus allowing sensitive detection of CG2a with a detection limit of 0.015 μM. Moreover, the fluorescence of igMFPs composed of the NIR-2/CG2a complex was remarkably enhanced with the increasing concentration of K^+ ion due to the stabilizing effect of K^+ ion on parallel G4 folding. The signal plateaued at 50 mM K^+ ion, implying that CG2a-derived igMFPs can be robustly formed at a physiological concentration of K^+ (100 mM) (Figure S33). We further characterized the effect of NIR-2 on the G4 stabilities of CG2a. CD spectra of CG2a were unchanged with NIR-2 treatment in the absence or the presence of K^+ (100 mM, Figure S34). Subsequent melting studies revealed that

https://doi.org/10.1021/jacs.1c04577
J. Am. Chem. Soc. XXXX, XXX, XXX−XXX

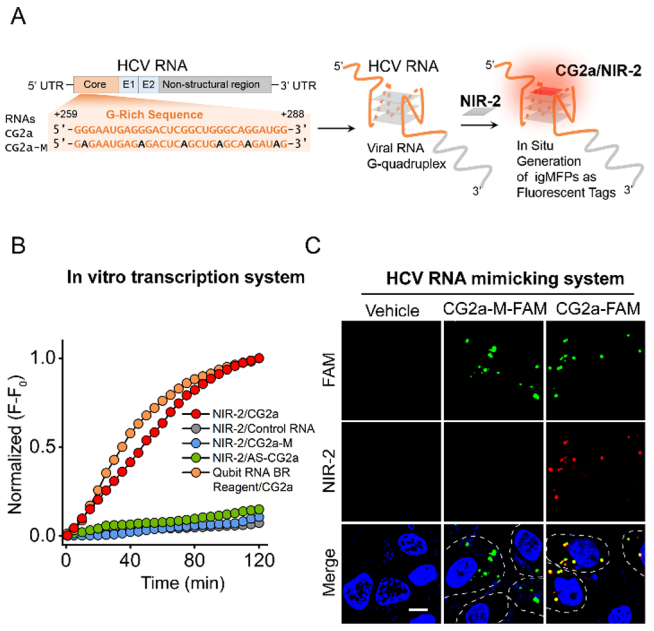

Figure 4. (A) Schematic illustration of in situ generation of igMFPs based on viral G-quadruplex in HCV RNA. (B) Fluorescence kinetics of in vitro transcription of control RNA, CG2a-Mut, CG2a, and CG2a with AS-CG2a in the presence of NIR-2 (10 μM) and CG2a in the presence of the Qubit RNA BR reagent (10×). (C) Confocal microscopy fluorescent imaging of the 1 μM NIR-2-stained Huh7 cells transfected with FAM-tagged CG2a RNA and FAM-tagged CG2a-M RNA, respectively. Scale bar: 10 μm.

NIR-2 slightly influenced G4 thermal stability of CG2a with or without K^+ (Figure S34). These results indicate that NIR-2 does not obviously interfere with G4 structural stability and perturb G4-folding dynamics.

Besides the synthetic CG2a, we also tested the RNA transcript of CG2a generated by the in vitro T7 RNA polymerase (T7RNAP) transcription system to mimic the RNA-generating mechanism in cellular conditions. Upon transcription initiation, NIR-2 shows a quick dynamic response to CG2a generation, similar to the reference RNA-staining dye (Qubit RNA BR). However, no detectable signal was observed upon the control RNA and the CG2a-Mut that are unable to form the G4 structure or the CG2a in the presence of the antisense strand AS-CG2a capable of blocking G4 formation via hybridization, revealing the fast response and high G4-specificity of NIR-2 (Figure 4B).

Visualization of Viral RNA in Living Cells via In Situ Formation of igMFPs. Encouraged by the promising in vitro results, we further investigate the performance of NIR-2 in live-cell imaging. At first, we transfect synthetic CG2a sequences into hepatocytes to simulate the HCV viral RNA-presenting cells (Figure 4C). Before the bioimaging experiments, the cell viability upon NIR-2 treatment for 24 h was evaluated by the MTT assay, which demonstrates NIR-2 has favorable biocompatibility (Figure S35). Subsequently, CG2a tagged with the fluorophore FAM was transfected into Huh7 cells, a hepatocyte-derived cellular carcinoma cell line widely investigated in HCV-relative research. Then, the transfected cells were stained by NIR-2. As shown in Figure 4C, the fluorescent puncta of NIR-2 (red) were clearly observed in the cytoplasm of CG2a-transfected Huh7 cells and colocalized well with the FAM signals (green) of CG2a (overlap coefficient, OLC = 0.91). In contrast, although GC2a-mut-transfected Huh7 cells show manifested GC2a-mut-FAM signals, no NIR-2 foci was observed. Thus, those results indicate that NIR-2 could efficiently recognize CG2a to form igMFPs in the live-cell context.

We next exploited a full-length HCV infectious cell line, GG2, to investigate whether the igMFPs generated by the NIR-2-bound viral G4 structure could be applied as an intrinsic tag for visualizing native viral RNA (Figure 5A). GG2 is a model cell line for HCV lifecycle research, which is derived from the aforesaid Huh7 cell line and enables the replication/translation of the full-length HCV 2a genome and the consequent production of virus particles.[57] GG2 and the control cell line Huh7 were stained with NIR-2 for comparison. In contrast to Huh7 cells without detectable fluorescent signals, GG2 cells show obvious punctate fluorescence foci of NIR-2 in its cytoplasm (Figure 5B and Figure S36), consistent with the quantitative reverse transcription PCR (RT-qPCR) results manifesting high-level production of HCV RNA genome in GG2 cells (Figure S37). These results revealed that igMFPs were formed and fluorescently activated only in NIR-2-treated HCV RNA-presenting cells. Moreover, to evaluate the effect of chromophores on imaging performance, we compared NIR-2 with its prototype DFHBFSI and the widely used, commercially available G4-specific dye ThT at the same incubation concentration (1 uM). As shown in Figure 5B and Figure S36, NIR-2 allowed quick staining with strong signals in GG2 cells within 10 min, whereas DFHBFSI and ThT-treated cells showed weak fluorescence even after 2 h, respectively. The superiority of NIR-2 in staining time probably results from (1) NIR-2 (logP = 4.85) is more hydrophobic than DFHBFSI (3.64) and ThT (4.29), and (2) NIR-2 is charge-neutral, unlike charged DFHBFSI and ThT, thus facilitating its cell membrane penetration (Table S5).

Subsequently, we determine whether the generation of igMFPs in GG2 cells originated from the specific targeting of NIR-2 to the G4 structure in the core gene of HCV viral RNA. Initial examinations were conducted using fixed GG2 cells. The fluorescent signal of NIR-2 disappeared upon treatment with RNase A but still existed after DNase I treatment, suggesting that these fluorescent foci are derived from RNA (Figure S38). The remarkably eliminated fluorescence of NIR-2 was also observed in the G-quadruplex ligand competition analysis using CarboxyPDS, a classical RNA G4-specific ligand, as a competitor, implying that the observed igMFPs might originate from the interaction of NIR-2 with RNA G4 structures (Figure S38). To precisely analyze the targeting site of NIR-2, two additional control cell lines were introduced: FCA1 cells, a core gene-deleted control cell line derived from Huh7 cells expressing the HCV RNA subgenome without the core gene region,[58] and GG2-G4-Mut cells, a G4-mutated control cell line expressing the full-length HCV 2a genome but introducing multiple point mutations into the G4-forming CG2a sequence (+265 to +279) of the core gene[53] (Figures S37 and S39). The targeting specificity of NIR-2 to the core gene of HCV RNA was evaluated using a specific molecular beacon (MB) probe with the FAM/BHQ1(fluorophore/quencher) pair for turn-on imaging of the conserved sequence (the position from +293 to +317) of the HCV core gene.[56,59] As shown in Figure 5C and Figure S40, upon the transfection of the beacon probe, the fluorescence foci of NIR-2 colocalized well with FAM signal of the core gene-activated MB in GG2 cells with an OLC of 0.89, but neither of them was present in the Huh7 and FCA1 cells

https://doi.org/10.1021/jacs.1c04577
J. Am. Chem. Soc. XXXX, XXX, XXX−XXX

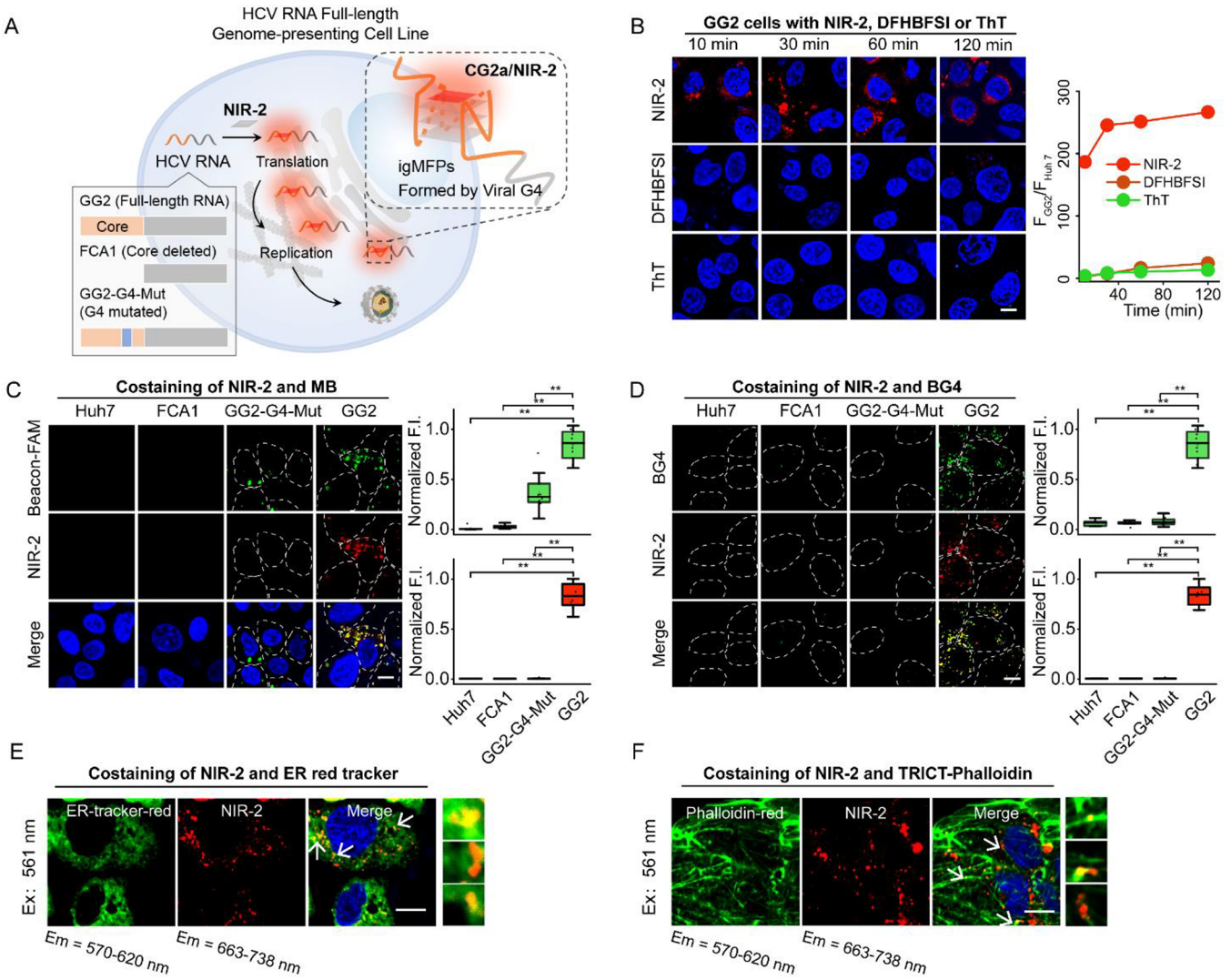

Figure 5. (A) Schematic illustration of igMFPs as fluorescence tags for tracking HCV RNA in the HCV full-length genome-presenting cell line. (B) Left: Confocal images of living GG2 cells at the indicated incubation times in the presence of NIR-2 (1 μM), DFHBFSI (1 μM), or ThT (1 μM). Scale bar: 10 μm. Right: The ratio of fluorescence intensity between GG2 and Huh7 cells at the indicated incubation times in the presence of NIR-2, DFHBFSI, and ThT, respectively. (C) Left: Confocal imaging of Beacon-FAM-transfected living Huh7, FCA1, GG2-G4-Mut, and GG2 cells in the presence of NIR-2 (1 μM). Scale bar: 10 μm. Right: Fluorescence intensities of Beacon-FAM and NIR-2 in Huh7, FCA-1, GG2-G4-Mut, and GG2 cells. Values represent means ± SD (n = 8), $^{**}p < 0.001$. (D) Left: Confocal images of the immunofluorescence staining of BG4 antibody and 1 μM NIR-2 staining in the fixed Huh7, FCA1, GG2-G4-Mut, and GG2 cells. Scale bar: 10 μm. Right: Fluorescence intensities of BG4 antibody and NIR-2 in Huh7, FCA-1, GG2-G4-Mut, and GG2 cells. Values represent means ± SD (n = 8), $^{**}p < 0.001$. Confocal imaging of GG2 cells stained with ER-red tracker (E) or TRICT-Phalloidin (F) in the presence of NIR-2 (1 μM). The images were acquired using 561 nm excitation and presented as merged images with a 570−620 nm emission channel for ER-red tracker (E) or TRICT-Phalloidin (F) and 663−738 nm emission channel for NIR-2. For clarity, the images were presented in pseudocolors of red (NIR-2) and green (ER-red tracker and TRICT-Phalloidin). Typical enlarged views of indicated regions in the left images are shown. Scale bar: 10 μm.

due to lack of the core gene. Only FAM spots of MB were observed in GG2-G4-Mut cells because GG2-G4-Mut cells express the whole core gene sequence but with the mutated G4-forming region. Flow cytometry data analysis also proved that NIR-2 selectively stained the GG2 cells, while negligible fluorescence was observed in Huh7, FCA1, or GG2-G4-Mut cells (Figure S41). Furthermore, we employed a G4-specific antibody BG4 in the immunofluorescence experiment to compare their intracellular localization with NIR-2-positive spots.[60,61] As evident from Figure 5D and Figure S42, NIR-2 foci show good colocalization with BG4 staining (OLC = 0.86) in the cytoplasm of GG2 cells, but negligible fluorescence signals of both NIR-2 and BG4 staining were observed in Huh7, FCA1, and GG2-G4-Mut cells. Further, the blockage of the G4 folding of the CG2a region in the HCV genome using AS-CG2a significantly eliminated both the fluorescence of NIR-2 and BG4 staining in the GG2 cells (Figure S43), indicating most of NIR-2 and BG4 foci was derived from viral G4s. Taken together, all results proved that the selective recognition of the innate G4 structure in the HCV core gene by NIR-2 accounted for the formation of igMFPs, presenting a potential intrinsic fluorescent tag for tracking HCV RNA.

To monitor detailed subcellular localizations of viral RNA in living cells, we multiplexed our igMFP system with different fluorescent trackers of specific cellular organelle or cytoskeleton in costaining experiments. ER Tracker red, an endoplasmic reticulum-specific probe, and Phalloidin red, a high-affinity probe for filamentous actin (F-actin), respectively, were

https://doi.org/10.1021/jacs.1c04577
J. Am. Chem. Soc. XXXX, XXX, XXX−XXX

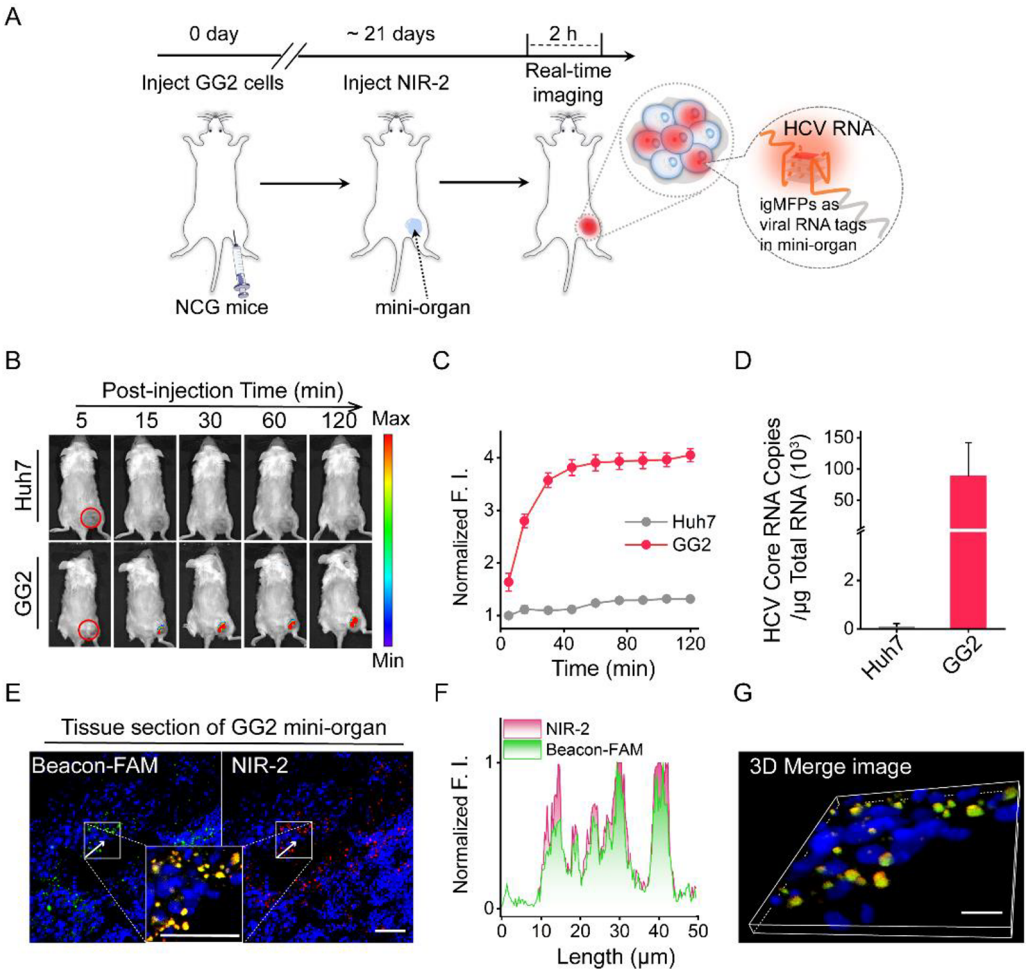

Figure 6. (A) Schematic illustration of igMFPs as fluorescence tags for real-time near-infrared fluorescence (NIRF) visualization of HCV RNA in vivo. (B) Real-time NIRF visualization of the NCG mice after injection of NIR-2 into the mini-organ embedded in the subcutaneous tissues. (C) Quantification of the NIRF signal in the mini-organ site as a function of postinjection time of NIR-2. (D) Quantitative-PCR analysis of the copy numbers of the HCV core gene in total RNA extracted from non-HCV RNA mini-organ (Huh7) and HCV RNA-presenting mini-organ (GG2). Values represent means ± SD (n = 4). (E) Confocal fluorescence images of HCV RNA-presenting mini-organ tissue slices after the incubation with Beacon-FAM and NIR-2. (1 μM). Scale bar: 50 μm. (F) Line-scan analysis to assess the spatial distribution of Beacon-FAM and NIR-2 in part E. (G) Three-dimensional reconstruction from the z-series of confocal images of the mini-organ tissue using image J software. Scale bar: 10 μm.

employed to costain the GG2 cells with NIR-2. Due to the NIR emission and large Stokes shift of NIR-2, the igMFP system is highly favorable to simultaneously image multicolor fluorophores. NIR-2 and the red-emissive probes, including ER Tracker red and Phalloidin red, were concurrently excited at the same 561 nm channel and monitored by separate emission channels of 570−620 nm and 663−738 nm, respectively, without obvious mutual interference. The result of confocal fluorescence imaging shows a good colocalization of NIR-2 foci and ER with a high OLC value of 0.64 (Figure 5E), which is consistent with the fact that the replication of HCV RNA genome and its package in virus particles occur primarily in ER-associated membrane.[62] We also found that most of the NIR-2 foci colocalized with or were in close proximity to the actin filaments (~71%) (Figure 5F), a major cytoskeleton component, attributed to the function of actin filaments as the tracks for the movement of HCV RNA replication complexes.[63] Together, these data suggest that our igMFP system could provide precise spatial information on the HCV RNA genome, presenting a potent tool for real-time analysis of the subcellular distribution of viral RNA in living cells.

Our above imaging results demonstrated that the NIR-2-staining-caused in situ formation of igMFPs is highly specific for imaging HCV RNA G4s in different cell models, including the mimicking system of viral RNA-presenting cells (Figure 4C) and the full-length HCV infectious cell line (Figure 5). Besides the intrinsic topologic specificity of NIR-2 for parallel G4s, other factors might account for this unique imaging specificity of igMFPs for viral RNA G4s, including (1) the significant difference in local concentration between HCV viral RNA G4 and endogenous host G4 caused by high expression level of viral RNA,[64,65] viral RNA enrichment induced by the replication complex-mediated confinement,[66,67] and the inhibition of endogenous DNA G4s by virus infection-mediated cell cycle arrest;[68] and (2) ultralow backgrounds from host endogenous G4s resulting from the moderate brightness and sensitivity, the cytoplasm-selective localization property, and the proper incubation conditions (low probe concentration of 1 μM and short incubation time of 10 min) of NIR-2. The detailed discussions are shown in the Supporting Information and Figures S44, S45, and S48.

In Vivo Imaging of Viral RNA in Living Mice. In light of the advantage of deep tissue penetrability of near-infrared

https://doi.org/10.1021/jacs.1c04577
J. Am. Chem. Soc. XXXX, XXX, XXX−XXX

fluorescence imaging and excellent performance in the cell imaging of the igMFP system, we further explore the feasibility of this system in vivo. First, we constructed a living animal model with HCV RNA-presenting or non-HCV RNA mini-organ by seeding the GG2 or Huh7 cells subcutaneously in NCG mice, a severely immuno-deficient humanized mice model widely used for human cell engraftment (Figure 6A). After orthotopic injection of NIR-2 in PBS into the mini-organ in living mice, the anesthetized mice were subjected to whole-body quantitative fluorescence imaging to acquire sequential images at different time points (Figure 6B). The mice bearing HCV RNA-presenting GG2 cells exhibited a significant enhancement of NIR-2 signal at the mini-organ site, whereas no obvious fluorescence was observed in the control mice bearing non-HCV RNA mini-organ, consistent with the results of the in cellular imaging. In particular, the NIR-2 signal in the HCV RNA-presenting mini-organ region was clearly observed at 15 min after NIR-2 injection and reaches the plateau after 30 min, implying the quick response of the NIR-2 probe owing to its small size favorable for tissue penetration, capability in fast permeating cell-membrane, and high affinity to the G4 target. Quantitation indicated that the mice bearing HCV RNA-presenting mini-organ presented a 3.4-fold higher NIR-2 signal than those with the non-HCV RNA control (Figure 6C). The active expression of HCV RNA in the HCV-RNA-presenting mini-organ was confirmed by the RT-qPCR results (Figure 6D), revealing the high replication level of the HCV viral core gene. The immunofluorescence analysis of mini-organ tissue samples indicates the remarkable translation level of an HCV RNA genome-encoding product, the nonstructural protein NS5A (Figure S46). These data strongly corroborate our in vivo imaging results, elaborating that the igMFP system is applicable for high-contrast in vivo imaging of HCV viral RNA.

In addition, the ex vivo histology of NIR-2-staining positive mini-organ was carried out to further confirm that the in situ generation of igMFPs in vivo relies on HCV RNA. The above-mentioned MB probe specific for the HCV core gene was used to track HCV viral RNA genome in the mini-organ. The spatial localization of HCV RNA in the tissue section of mini-organ was synchronously assessed by 3D colocalization analysis between the signals of NIR-2 and FAM of the activated MB. As shown in Figure 6E−G, the fluorescence signal of NIR-2 was seen in the tissue slice of the HCV RNA-presenting mini-organ, consistent with the in vivo imaging data. Notably, the NIR-2 signal shows an excellent overlap coefficient of 0.88 with the FAM signal of MB in every section, whereas neither signals appear in the control mini-organ (Figure S47), proving the precise HCV RNA imaging by igMFPs in living mice.

CONCLUSION

In summary, we proposed a "D−A−A′" rationale for molecular tailoring of GFP chromophore analogues to develop NIR-emissive mimics of fluorescent proteins, which unprecedentedly surpass the inherent limitation of existing GFP-like fluorescent proteins and their artificial mimics on emission wavelength. The introduction of dialkylaminobenzyl and quinoline groups as D and A′ moieties cause the elongated "push-pull" electronic conjugation with enhanced ICT process, affording the FP chromophore analogues exhibiting a significant emission shift to the NIR region. These new fluorogenic chromophores can specifically target and fluorescently light-up G4 structures to form igMFPs, providing a potential NIR-emissive fluorescent tag for nucleic acid bioimaging. Compared with infrared fluorescent proteins, igMFPs possess higher quantum yields, larger Stokes shift, and better photostability. As a proof-of-concept application, we exploited pathogen-related G4 as the target and successfully applied igMFPs to directly visualize native HCV RNA genome in living cells via their in situ formation by the chromophore-bound viral G4 structure in the HCV core gene. Furthermore, igMFPs are feasible for high contrast HCV RNA imaging in living animals bearing HCV RNA-presenting mini-organ, presenting the first time, to our knowledge, that FP mimics have been employed for whole-body imaging. In addition, NIR-2 is also the first near-infrared G4 probe achieving intracellular G4 imaging in living animals (detailed comparison with existing NIR-emissive G4 probes is shown in Table S7) and visualization of the native viral RNA genome in cellula and in vivo. Given its unique dual engineering properties, our igMFP system affords a highly modular scaffold with superior extendibility, which allows further expansion of the spectral palette and optimization of photophysical properties via molecular engineering of chromophores, or improvement of target adaptivity, specificity, and multiplicity by rational design or directed evolution of nucleic acid hosts. Hence, we envision that the NIR-emissive nucleic acid mimics of FPs would present a promising toolkit for spatiotemporal analysis of nucleic acids-of-interest in intact animals, which hold great potential in clinical diagnosis and pathological research.

ASSOCIATED CONTENT

Supporting Information

The Supporting Information is available free of charge at https://pubs.acs.org/doi/10.1021/jacs.1c04577.

Experimental procedures; supplementary tables (Tables S1−S6), schemes (Schemes S1−S3), and figures (Figures S1−S48); characterization of new compounds; and discussion of the specificity of igMFPs for viral RNA G4s imaging (PDF)

AUTHOR INFORMATION

Corresponding Author

Zhou Nie − *State Key Laboratory of Chemo/Biosensing and Chemometrics, College of Chemistry and Chemical Engineering, Hunan Provincial Key Laboratory of Biomacromolecular Chemical Biology, Hunan University, Changsha 410082, People's Republic of China;* orcid.org/0000-0001-9864-2965; Email: niezhou.hnu@gmail.com

Authors

Jiaheng Zhang − *State Key Laboratory of Chemo/Biosensing and Chemometrics, College of Chemistry and Chemical Engineering, Hunan Provincial Key Laboratory of Biomacromolecular Chemical Biology, Hunan University, Changsha 410082, People's Republic of China*

Huiyi Li − *Institute of Pathogen Biology and Immunology of College of Biology, State Key Laboratory of Chemo/Biosensing and Chemometrics, Hunan University, Changsha 410082, People's Republic of China*

Bin Lin − *Pharmaceutical Engineering & Key Laboratory of Structure-Based Drug Design & Discovery, Ministry of Education, Shenyang Pharmaceutical University, Shenyang 110016, People's Republic of China*

Xingyu Luo − *State Key Laboratory of Chemo/Biosensing and Chemometrics, College of Chemistry and Chemical*

https://doi.org/10.1021/jacs.1c04577
J. Am. Chem. Soc. XXXX, XXX, XXX−XXX

Engineering, Hunan Provincial Key Laboratory of Biomacromolecular Chemical Biology, Hunan University, Changsha 410082, People's Republic of China; orcid.org/0000-0001-7219-0921

Peng Yin − *State Key Laboratory of Chemo/Biosensing and Chemometrics, College of Chemistry and Chemical Engineering, Hunan Provincial Key Laboratory of Biomacromolecular Chemical Biology, Hunan University, Changsha 410082, People's Republic of China*

Ting Yi − *State Key Laboratory of Chemo/Biosensing and Chemometrics, College of Chemistry and Chemical Engineering, Hunan Provincial Key Laboratory of Biomacromolecular Chemical Biology, Hunan University, Changsha 410082, People's Republic of China*

Binbin Xue − *Institute of Pathogen Biology and Immunology of College of Biology, State Key Laboratory of Chemo/Biosensing and Chemometrics, Hunan University, Changsha 410082, People's Republic of China*

Xiao-Lian Zhang − *State Key Laboratory of Virology and Hubei Province Key Laboratory of Allergy and Immunology and Department of Immunology, School of Medicine, Wuhan University, Wuhan 430071 Hubei, People's Republic of China;* orcid.org/0000-0002-8283-9381

Haizhen Zhu − *Institute of Pathogen Biology and Immunology of College of Biology, State Key Laboratory of Chemo/Biosensing and Chemometrics, Hunan University, Changsha 410082, People's Republic of China*

Complete contact information is available at: https://pubs.acs.org/10.1021/jacs.1c04577

Author Contributions

[⊥]Jiaheng Zhang and Huiyi Li contributed equally.

Notes

The authors declare no competing financial interest.

■ ACKNOWLEDGMENTS

This work was supported by the National Natural Science Foundation of China (Grant Nos. 22034002 and 21725503) and the National Key Research and Development Program of China (Grant 2020YFA0907500). We thank Prof. Lin Yuan and Dr. Tianbing Ren for helpful discussion about the theoretical calculations.

■ REFERENCES

(1) Day, R. N.; Davidson, M. W. The fluorescent protein palette: tools for cellular imaging. *Chem. Soc. Rev.* **2009**, *38* (10), 2887−2921.
(2) Hoffman, R. M. The multiple uses of fluorescent proteins to visualize cancer in vivo. *Nat. Rev. Cancer* **2005**, *5* (10), 796−806.
(3) Newman, R. H.; Fosbrink, M. D.; Zhang, J. Genetically Encodable Fluorescent Biosensors for Tracking Signaling Dynamics in Living Cells. *Chem. Rev.* **2011**, *111* (5), 3614−3666.
(4) Nienhaus, K.; Ulrich Nienhaus, G. Fluorescent proteins for live-cell imaging with super-resolution. *Chem. Soc. Rev.* **2014**, *43* (4), 1088−1106.
(5) Deng, H. H.; Yan, S. T.; Huang, Y.; Lei, C. Y.; Nie, Z. Design strategies for fluorescent proteins/mimics and their applications in biosensing and bioimaging. *TrAC, Trends Anal. Chem.* **2020**, *122*, 115757.
(6) Weissleder, R. A clearer vision for in vivo imaging. *Nat. Biotechnol.* **2001**, *19* (4), 316−317.
(7) Guo, Z. Q.; Park, S.; Yoon, J.; Shin, I. Recent progress in the development of near-infrared fluorescent probes for bioimaging applications. *Chem. Soc. Rev.* **2014**, *43* (1), 16−29.
(8) East, A. K.; Lucero, M. Y.; Chan, J. New directions of activity-based sensing for in vivo NIR imaging. *Chem. Sci.* **2021**, *12* (10), 3393−3405.
(9) Ng, H. L.; Lin, M. Z. Structure-guided wavelength tuning in far-red fluorescent proteins. *Curr. Opin. Struct. Biol.* **2016**, *39*, 124−133.
(10) Shcherbakova, D. M.; Subach, O. M.; Verkhusha, V. V. Red Fluorescent Proteins: Advanced Imaging Applications and Future Design. *Angew. Chem., Int. Ed.* **2012**, *51* (43), 10724−10738.
(11) Shaner, N. C.; Campbell, R. E.; Steinbach, P. A.; Giepmans, B. N. G.; Palmer, A. E.; Tsien, R. Y. Improved monomeric red, orange and yellow fluorescent proteins derived from Discosoma sp red fluorescent protein. *Nat. Biotechnol.* **2004**, *22* (12), 1567−1572.
(12) Shu, X. K.; Royant, A.; Lin, M. Z.; Aguilera, T. A.; Lev-Ram, V.; Steinbach, P. A.; Tsien, R. Y. Mammalian Expression of Infrared Fluorescent Proteins Engineered from a Bacterial Phytochrome. *Science* **2009**, *324* (5928), 804−807.
(13) Walker, C. L.; Lukyanov, K. A.; Yampolsky, I. V.; Mishin, A. S.; Bommarius, A. S.; Duraj-Thatte, A. M.; Azizi, B.; Tolbert, L. M.; Solntsev, K. M. Fluorescence imaging using synthetic GFP chromophores. *Curr. Opin. Chem. Biol.* **2015**, *27*, 64−74.
(14) Chatterjee, S.; Ahire, K.; Karuso, P. Room-Temperature Dual Fluorescence of a Locked Green Fluorescent Protein Chromophore Analogue. *J. Am. Chem. Soc.* **2020**, *142* (2), 738−749.
(15) Myasnyanko, I. N.; Gavrikov, A. S.; Zaitseva, S. O.; Smirnov, A. Y.; Zaitseva, E. R.; Sokolov, A. I.; Malyshevskaya, K. K.; Baleeva, N. S.; Mishin, A. S.; Baranov, M. S. Color Tuning of Fluorogens for FAST Fluorogen-Activating Protein. *Chem. - Eur. J.* **2021**, *27* (12), 3986−3990.
(16) Baranov, M. S.; Lukyanov, K. A.; Borissova, A. O.; Shamir, J.; Kosenkov, D.; Slipchenko, L. V.; Tolbert, L. M.; Yampolsky, I. V.; Solntsev, K. M. Conformationally Locked Chromophores as Models of Excited-State Proton Transfer in Fluorescent Proteins. *J. Am. Chem. Soc.* **2012**, *134* (13), 6025−6032.
(17) Chang, J.; Romei, M. G.; Boxer, S. G. Structural Evidence of Photoisomerization Pathways in Fluorescent Proteins. *J. Am. Chem. Soc.* **2019**, *141* (39), 15504−15508.
(18) Hsu, Y. H.; Chen, Y. A.; Tseng, H. W.; Zhang, Z. Y.; Shen, J. Y.; Chuang, W. T.; Lin, T. C.; Lee, C. S.; Hung, W. Y.; Hong, B. C.; Liu, S. H.; Chou, P. T. Locked ortho- and para-Core Chromophores of Green Fluorescent Protein; Dramatic Emission Enhancement via Structural Constraint. *J. Am. Chem. Soc.* **2014**, *136* (33), 11805−11812.
(19) Baldridge, A.; Samanta, S. R.; Jayaraj, N.; Ramamurthy, V.; Tolbert, L. M. Steric and Electronic Effects in Capsule-Confined Green Fluorescent Protein Chromophores. *J. Am. Chem. Soc.* **2011**, *133* (4), 712−715.
(20) Williams, D. E.; Dolgopolova, E. A.; Pellechia, P. J.; Palukoshka, A.; Wilson, T. J.; Tan, R.; Maier, J. M.; Greytak, A. B.; Smith, M. D.; Krause, J. A.; Shustova, N. B. Mimic of the Green Fluorescent Protein beta-Barrel: Photophysics and Dynamics of Confined Chromophores Defined by a Rigid Porous Scaffold. *J. Am. Chem. Soc.* **2015**, *137* (6), 2223−2226.
(21) Baldridge, A.; Feng, S. H.; Chang, Y. T.; Tolbert, L. M. Recapture of GFP Chromophore Fluorescence in a Protein Host. *ACS Comb. Sci.* **2011**, *13* (3), 214−217.
(22) Liu, Y.; Wolstenholme, C. H.; Carter, G. C.; Liu, H. B.; Hu, H.; Grainger, L. S.; Miao, K.; Fares, M.; Hoelzel, C. A.; Yennawar, H. P.; Ning, G.; Du, M. Y.; Bai, L.; Li, X. S.; Zhang, X. Modulation of Fluorescent Protein Chromophores To Detect Protein Aggregation with Turn-On Fluorescence. *J. Am. Chem. Soc.* **2018**, *140* (24), 7381−7384.
(23) Steinmetzger, C.; Bessi, I.; Lenz, A. K.; Hobartner, C. Structure-fluorescence activation relationships of a large Stokes shift fluorogenic RNA aptamer. *Nucleic Acids Res.* **2019**, *47* (22), 11538−11550.
(24) Deng, H. P.; Zhu, X. Y. Emission enhancement and application of synthetic green fluorescent protein chromophore analogs. *Mater. Chem. Front* **2017**, *1* (4), 619−629.

(25) You, M. X.; Jaffrey, S. R. Structure and Mechanism of RNA Mimics of Green Fluorescent Protein. *Annu. Rev. Biophys.* **2015**, *44*, 187−206.
(26) Truong, L.; Ferre-D'Amare, A. R. From fluorescent proteins to fluorogenic RNAs: Tools for imaging cellular macromolecules. *Protein Sci.* **2019**, *28* (8), 1374−1386.
(27) Paige, J. S.; Wu, K. Y.; Jaffrey, S. R. RNA Mimics of Green Fluorescent Protein. *Science* **2011**, *333* (6042), 642−646.
(28) Song, W. J.; Filonov, G. S.; Kim, H.; Hirsch, M.; Li, X.; Moon, J. D.; Jaffrey, S. R. Imaging RNA polymerase III transcription using a photostable RNA-fluorophore complex. *Nat. Chem. Biol.* **2017**, *13* (11), 1187−1194.
(29) Strack, R. L.; Disney, M. D.; Jaffrey, S. R. A superfolding Spinach2 reveals the dynamic nature of trinucleotide repeat-containing RNA. *Nat. Methods* **2013**, *10* (12), 1219−1124.
(30) Karunanayake Mudiyanselage, A. P. K. K.; Yu, Q.; Leon-Duque, M. A.; Zhao, B.; Wu, R.; You, M. Genetically Encoded Catalytic Hairpin Assembly for Sensitive RNA Imaging in Live Cells. *J. Am. Chem. Soc.* **2018**, *140* (28), 8739−8745.
(31) Litke, J. L.; Jaffrey, S. R. Highly efficient expression of circular RNA aptamers in cells using autocatalytic transcripts. *Nat. Biotechnol.* **2019**, *37* (6), 667−675.
(32) Li, X.; Kim, H.; Litke, J. L.; Wu, J. H.; Jaffrey, S. R. Fluorophore-Promoted RNA Folding and Photostability Enables Imaging of Single Broccoli-Tagged mRNAs in Live Mammalian Cells. *Angew. Chem., Int. Ed.* **2020**, *59* (11), 4511−4518.
(33) Feng, G. F.; Luo, C.; Yi, H. B.; Yuan, L.; Lin, B.; Luo, X. Y.; Hu, X. X.; Wang, H. H.; Lei, C. Y.; Nie, Z.; Yao, S. Z. DNA mimics of red fluorescent proteins (RFP) based on G-quadruplex-confined synthetic RFP chromophores. *Nucleic Acids Res.* **2017**, *45* (18), 10380−10392.
(34) Ando, R.; Hama, H.; Yamamoto-Hino, M.; Mizuno, H.; Miyawaki, A. An optical marker based on the UV-induced green-to-red photoconversion of a fluorescent protein. *Proc. Natl. Acad. Sci. U. S. A.* **2002**, *99* (20), 12651−12656.
(35) Chen, C.; Baranov, M. S.; Zhu, L. D.; Baleeva, N. S.; Smirnov, A. Y.; Zaitseva, S. O.; Yampolsky, I. V.; Solntsev, K. M.; Fang, C. Designing redder and brighter fluorophores by synergistic tuning of ground and excited states. *Chem. Commun.* **2019**, *55* (17), 2537−2540.
(36) Wang, L. L.; Du, W.; Hu, Z. J.; Uvdal, K.; Li, L.; Huang, W. Hybrid Rhodamine Fluorophores in the Visible/NIR Region for Biological Imaging. *Angew. Chem., Int. Ed.* **2019**, *58* (40), 14026−14043.
(37) Feng, G. F.; Luo, X. Y.; Lu, X.; Xie, S. Y.; Deng, L.; Kang, W. Y.; He, F.; Zhang, J. H.; Lei, C. Y.; Lin, B.; Huang, Y.; Nie, Z.; Yao, S. Z. Engineering of Nucleic Acids and Synthetic Cofactors as Holo Sensors for Probing Signaling Molecules in the Cellular Membrane Microenvironment. *Angew. Chem., Int. Ed.* **2019**, *58* (20), 6590−6594.
(38) Grabowski, Z. R.; Rotkiewicz, K.; Rettig, W. Structural changes accompanying intramolecular electron transfer: Focus on twisted intramolecular charge-transfer states and structures. *Chem. Rev.* **2003**, *103* (10), 3899−4031.
(39) Siddiqui-Jain, A.; Grand, C. L.; Bearss, D. J.; Hurley, L. H. Direct evidence for a G-quadruplex in a promoter region and its targeting with a small molecule to repress c-MYC transcription. *Proc. Natl. Acad. Sci. U. S. A.* **2002**, *99* (18), 11593−11598.
(40) Wolstenholme, C. H.; Hu, H.; Ye, S. T.; Funk, B. E.; Jain, D.; Hsiung, C. H.; Ning, G.; Liu, Y.; Li, X. S.; Zhang, X. AggFluor: Fluorogenic Toolbox Enables Direct Visualization of the Multi-Step Protein Aggregation Process in Live Cells. *J. Am. Chem. Soc.* **2020**, *142* (41), 17515−17523.
(41) Ye, S. T.; Zhang, H.; Fei, J. Y.; Wolstenholme, C. H.; Zhang, X. A General Strategy to Control Viscosity Sensitivity of Molecular Rotor-Based Fluorophores. *Angew. Chem., Int. Ed.* **2021**, *60* (3), 1339−1346.
(42) Qian, H.; Cousins, M. E.; Horak, E. H.; Wakefield, A.; Liptak, M. D.; Aprahamian, I. Suppression of Kasha's rule as a mechanism for fluorescent molecular rotors and aggregation-induced emission. *Nat. Chem.* **2017**, *9* (1), 83−87.
(43) Olsen, S.; Smith, S. C. Radiationless decay of red fluorescent protein chromophore models via twisted intramolecular charge-transfer states. *J. Am. Chem. Soc.* **2007**, *129* (7), 2054−2065.
(44) Martin, M. E.; Negri, F.; Olivucci, M. Origin, nature, and fate of the fluorescent state of the green fluorescent protein chromophore at the CASPT2//CASSCF resolution. *J. Am. Chem. Soc.* **2004**, *126* (17), 5452−5464.
(45) Su, D.; Teoh, C. L.; Wang, L.; Liu, X.; Chang, Y. T. Motion-induced change in emission (MICE) for developing fluorescent probes. *Chem. Soc. Rev.* **2017**, *46* (16), 4833−4844.
(46) Tian, T.; Chen, Y. Q.; Wang, S. R.; Zhou, X. G-Quadruplex: A Regulator of Gene Expression and Its Chemical Targeting. *Chem-Us* **2018**, *4* (6), 1314−1344.
(47) Wang, X. L.; Huang, J.; Zhou, Y. Y.; Yan, S. Y.; Weng, X. C.; Wu, X. J.; Deng, M. G.; Zhou, X. A. Conformational Switching of G-Quadruplex DNA by Photoregulation. *Angew. Chem., Int. Ed.* **2010**, *49* (31), 5305−5309.
(48) Nadai, M.; Doria, F.; Scalabrin, M.; Pirota, V.; Grande, V.; Bergamaschi, G.; Amendola, V.; Winnerdy, F. R.; Phan, A. T.; Richter, S. N.; Freccero, M. A Catalytic and Selective Scissoring Molecular Tool for Quadruplex Nucleic Acids. *J. Am. Chem. Soc.* **2018**, *140* (44), 14528−14532.
(49) Chambers, V. S.; Marsico, G.; Boutell, J. M.; Di Antonio, M.; Smith, G. P.; Balasubramanian, S. High-throughput sequencing of DNA G-quadruplex structures in the human genome. *Nat. Biotechnol.* **2015**, *33* (8), 877−881.
(50) Di Antonio, M.; Ponjavic, A.; Radzevicius, A.; Ranasinghe, R. T.; Catalano, M.; Zhang, X. Y.; Shen, J. Z.; Needham, L. M.; Lee, S. F.; Klenerman, D.; Balasubramanian, S. Single-molecule visualization of DNA G-quadruplex formation in live cells. *Nat. Chem.* **2020**, *12* (9), 832−836.
(51) Lat, P. K.; Liu, K.; Kumar, D. N.; Wong, K. K. L.; Verheyen, E. M.; Sen, D. High specificity and tight spatial restriction of self-biotinylation by DNA and RNA G-Quadruplexes complexed in vitro and in vivo with Heme. *Nucleic Acids Res.* **2020**, *48* (10), 5254−5267.
(52) Ruggiero, E.; Richter, S. N. G-quadruplexes and G-quadruplex ligands: targets and tools in antiviral therapy. *Nucleic Acids Res.* **2018**, *46* (7), 3270−3283.
(53) Wang, S. R.; Min, Y. Q.; Wang, J. Q.; Liu, C. X.; Fu, B. S.; Wu, F.; Wu, L. Y.; Qiao, Z. X.; Song, Y. Y.; Xu, G. H.; Wu, Z. G.; Huang, G.; Peng, N. F.; Huang, R.; Mao, W. X.; Peng, S.; Chen, Y. Q.; Zhu, Y.; Tian, T.; Zhang, X. L.; Zhou, X. A highly conserved G-rich consensus sequence in hepatitis C virus core gene represents a new anti-hepatitis C target. *Sci. Adv.* **2016**, *2* (4), No. e1501535.
(54) Zhao, C. Q.; Qin, G.; Niu, J. S.; Wang, Z.; Wang, C. Y.; Ren, J. S.; Qu, X. G. Targeting RNA G-Quadruplex in SARS-CoV-2: A Promising Therapeutic Target for COVID-19? *Angew. Chem., Int. Ed.* **2021**, *60* (1), 432−438.
(55) Murat, P.; Zhong, J.; Lekieffre, L.; Cowieson, N. P.; Clancy, J. L.; Preiss, T.; Balasubramanian, S.; Khanna, R.; Tellam, J. G-quadruplexes regulate Epstein-Barr virus-encoded nuclear antigen 1 mRNA translation. *Nat. Chem. Biol.* **2014**, *10* (5), 358−364.
(56) Luo, X. Y.; Xue, B. B.; Feng, G. F.; Zhang, J. H.; Lin, B.; Zeng, P.; Li, H. Y.; Yi, H. B.; Zhang, X. L.; Zhu, H. Z.; Nie, Z. Lighting up the Native Viral RNA Genome with a Fluorogenic Probe for the Live-Cell Visualization of Virus Infection. *J. Am. Chem. Soc.* **2019**, *141* (13), 5182−5191.
(57) Qin, Y.; Xue, B.; Liu, C.; Wang, X.; Tian, R.; Xie, Q.; Guo, M.; Li, G.; Yang, D.; Zhu, H. NLRX1Mediates MAVS Degradation To Attenuate the Hepatitis C Virus-Induced Innate Immune Response through PCBP2. *J. Virol.* **2017**, *91* (23), No. e01264-17.
(58) Xue, B. B.; Yang, D. R.; Wang, J. J.; Xu, Y.; Wang, X. H.; Qin, Y. W.; Tian, R. Y.; Chen, S. W.; Xie, Q. Y.; Liu, N. L.; Zhu, H. Z. ISG12a Restricts Hepatitis C Virus Infection through the Ubiquitination-Dependent Degradation Pathway. *J. Virol.* **2016**, *90* (15), 6832−6845.
(59) Yu, R.; Yang, D.; Lei, S.; Wang, X.; Meng, X.; Xue, B.; Zhu, H. HMGB1 Promotes Hepatitis C Virus Replication by Interaction with Stem-Loop 4 in the Viral 5′ Untranslated Region. *J. Virol.* **2016**, *90* (5), 2332−2344.

https://doi.org/10.1021/jacs.1c04577
J. Am. Chem. Soc. XXXX, XXX, XXX−XXX

(60) Biffi, G.; Di Antonio, M.; Tannahill, D.; Balasubramanian, S. Visualization and selective chemical targeting of RNA G-quadruplex structures in the cytoplasm of human cells. *Nat. Chem.* **2014**, *6* (1), 75−80.
(61) Chen, X. C.; Chen, S. B.; Dai, J.; Yuan, J. H.; Ou, T. M.; Huang, Z. S.; Tan, J. H. Tracking the Dynamic Folding and Unfolding of RNA G-Quadruplexes in Live Cells. *Angew. Chem., Int. Ed.* **2018**, *57* (17), 4702−4706.
(62) Shulla, A.; Randall, G. Spatiotemporal Analysis of Hepatitis C Virus Infection. *PLoS Pathog.* **2015**, *11* (3), No. e1004758.
(63) Lai, C. K.; Jeng, K. S.; Machida, K.; Lai, M. M. C. Association of hepatitis C virus replication complexes with microtubules and actin filaments is dependent on the interaction of NS3 and NS5A. *J. Virol.* **2008**, *82* (17), 8838−8848.
(64) Zhang, Y.-Y.; Zhang, B.-H.; Ishii, K.; Liang, T. J. Novel Function of CD81 in Controlling Hepatitis C Virus Replication. *J. Virol.* **2010**, *84* (7), 3396−3407.
(65) Bukh, J. The history of hepatitis C virus (HCV): Basic research reveals unique features in phylogeny, evolution and the viral life cycle with new perspectives for epidemic control. *J. Hepatol.* **2016**, *65* (1), S2−S21.
(66) Lohmann, V.; Bartenschlager, R. E. Hepatitis C Virus RNA Replication. In *Hepatitis C Virus: From Molecular Virology to Antiviral Therapy*; Springer: Berlin, Germany, 2013; Vol. *369*, pp 167−198.
(67) Suzuki, T.; Tagaya, M.; Simmen, T. Hepatitis C Virus Replication. In *Organelle Contact Sites: From Molecular Mechanism to Disease*; Springer: Singapore, 2017; Vol. *997*, pp 199−209.
(68) Walters, K.-A.; Syder, A. J.; Lederer, S. L.; Diamond, D. L.; Paeper, B.; Rice, C. M.; Katze, M. G. Genomic Analysis Reveals a Potential Role for Cell Cycle Perturbation in HCV-Mediated Apoptosis of Cultured Hepatocytes. *PLoS Pathog.* **2009**, *5* (1), No. e1000269.

https://doi.org/10.1021/jacs.1c04577
J. Am. Chem. Soc. XXXX, XXX, XXX−XXX